

# Supercritical CO<sub>2</sub>-Assisted SiO<sub>x</sub>/Carbon Multi-Layer Coating on Si Anode for Lithium-Ion Batteries

Rahmandhika Firdauzha Hary Hernandha, Purna Chandra Rath, Bharath Umesh, Jagabandhu Patra, Chih-Yang Huang, Wen-Wei Wu, Quan-Feng Dong, Ju Li, and Jeng-Kuei Chang\*

Supercritical CO<sub>2</sub> (SCCO<sub>2</sub>), characterized by gas-like diffusivity, low surface tension, and excellent mass transfer properties, is applied to create a SiO<sub>x</sub>/carbon multi-layer coating on Si particles. Interaction of SCCO<sub>2</sub> with Si produces a continuous SiO<sub>x</sub> layer, which can buffer Si volume change during lithiation/delithiation. In addition, a conformal carbon film is deposited around the Si@SiO<sub>x</sub> core. Compared to the carbon film produced via a conventional wet-chemical method, the SCCO<sub>2</sub>-deposited carbon has significantly fewer oxygen-containing functional groups and thus higher electronic conductivity. Three types of carbon precursors, namely, glucose, sucrose, and citric acid, in the SCCO<sub>2</sub> syntheses are compared. An eco-friendly, cost-effective, and scalable SCCO<sub>2</sub> process is thus developed for the single-step production of a unique Si@SiO<sub>x</sub>@C anode for Li-ion batteries. The sample prepared using the glucose precursor shows the highest tap density, the lowest charge transfer resistance, and the best Li<sup>+</sup> transport kinetics among the electrodes, resulting in a high specific capacity of 918 mAh g<sup>-1</sup> at 5 A g<sup>-1</sup>. After 300 charge–discharge cycles, the electrode retains its integrity and the accumulation of the solid electrolyte interphase is low. The great potential of the proposed SCCO<sub>2</sub> synthesis and composite anode for Li-ion battery applications is demonstrated.

carbonaceous anode (e.g., graphite).<sup>[3]</sup> However, a graphite anode, whose theoretical capacity is limited to 372 mAh g<sup>-1</sup>, cannot meet the escalating application requirements. To improve LIB performance, several high-capacity anodes such as, those made of transition metal oxides, Si, Sn, Sb, Al, Mg, Bi, and their alloys have been studied.<sup>[4]</sup> Among them, Si is a promising anode material due to its high gravimetric capacity (theoretically 3579 mAh g<sup>-1</sup>), earth abundance, and low toxicity.<sup>[5]</sup> Moreover, its relatively high lithiation/delithiation potential compared to that of graphite makes it safer to operate (i.e., lower risk of Li metal plating).<sup>[6]</sup> Thus, Si-based anodes have the potential for application in high-performance, eco-friendly, and low-cost LIBs. Nevertheless, the practical implementation of Si anodes is hindered by its fast capacity decay.<sup>[7]</sup> The severe volume change (i.e., ~400%) of Si during lithiation/delithiation causes the mechanical degradation and pulverization of Si particles. Repeated volume expansion/contraction also results in an unstable solid electrolyte interphase (SEI). Low Coulombic efficiency (CE) and SEI accumulation gradually increase the interfacial resistance, leading to electrode performance decay.<sup>[8]</sup>

To prevent the fast degradation of Si anode, several strategies have been investigated, including size and morphology control,<sup>[9]</sup> nano-architecture design,<sup>[10]</sup> application of composites/hybrids,<sup>[11]</sup> and binder optimization.<sup>[12]</sup> A thin, uniform,


SEI layer is essential for maintaining the structural integrity of Si particles during lithiation/delithiation. In this work, we report a novel SCCO<sub>2</sub>-assisted synthesis of a Si@SiO<sub>x</sub>@C anode for Li-ion batteries. The Si@SiO<sub>x</sub>@C anode shows a high specific capacity of 918 mAh g<sup>-1</sup> at 5 A g<sup>-1</sup> and excellent cycle life after 300 cycles. The great potential of the proposed SCCO<sub>2</sub> synthesis and composite anode for Li-ion battery applications is demonstrated.

## 1. Introduction

To meet the surging demand for portable electronic devices and electric vehicles, efficient energy storage devices with high energy and power densities are urgently required. Lithium-ion batteries (LIBs) currently fill this need. However, despite decades of progress, the capacity and cycle life of LIBs remain unsatisfactory.<sup>[1,2]</sup> LIBs commonly use a conventional

R. F. H. Hernandha, Dr. P. C. Rath, Dr. J. Patra, C.-Y. Huang, Prof. W.-W. Wu, Prof. J.-K. Chang  
Department of Materials Science and Engineering  
National Yang Ming Chiao Tung University  
1001 University Road, Hsinchu 30010, Taiwan  
E-mail: jkchang@nctu.edu.tw

B. Umesh, Prof. J.-K. Chang  
Institute of Materials Science and Engineering  
National Central University  
300 Jhong-Da Road, Taoyuan 32001, Taiwan

 The ORCID identification number(s) for the author(s) of this article can be found under <https://doi.org/10.1002/adfm.202104135>.

DOI: 10.1002/adfm.202104135

Dr. J. Patra, Prof. J.-K. Chang  
Hierarchical Green-Energy Materials (Hi-GEM) Research Center  
National Cheng Kung University  
1 University Road, Tainan 70101, Taiwan

Prof. Q.-F. Dong  
State Key Laboratory for Physical Chemistry of Solid Surfaces  
Department of Chemistry  
Xiamen University  
Xiamen 361005, China

Prof. J. Li  
Department of Nuclear Science and Engineering and Department of Materials Science and Engineering  
Massachusetts Institute of Technology  
77 Massachusetts Avenue, Cambridge, MA 02139, USA

and conformal carbon layer on the Si surface is highly desirable to boost Si conductivity and stabilize the interface. However, a conventional wet-chemical carbon coating method cannot form a high-quality surface covering layer.<sup>[13]</sup> Because of the high surface tension of the liquid reaction medium, Si aggregates are not easily dispersed, and thus carbon precursors are not effectively delivered between Si nanoparticles.<sup>[14]</sup> More advanced gas-phase carbon coating processes have thus been employed for Si particles. Magnetron sputtering deposition,<sup>[15]</sup> atomic/molecular layer deposition,<sup>[16]</sup> and pulsed laser deposition<sup>[17,18]</sup> have been applied to improve coating quality. However, these techniques require sophisticated facilities, complicate procedures, and high cost, which hinder their practical applications. A more facile, cost-effective, eco-friendly, and easily scalable carbon coating process is required. A SiO<sub>x</sub> coating can improve Si anode cycling stability.<sup>[19]</sup> SiO<sub>x</sub> shows a smaller volume change during lithiation/delithiation compared to that of Si. Moreover, the Li<sub>2</sub>O and lithium silicates in situ generated during the first lithiation buffer the volume variation and thus improve cyclability.<sup>[20]</sup> Nevertheless, creating a continuous and homogeneous SiO<sub>x</sub> coating layer is challenging and usually needs extra synthesis procedures. The formation of a SiO<sub>x</sub>/carbon multi-layer coating in one step, the goal of the present work, is thus highly desirable.

In this context, we believe that supercritical carbon dioxide (SCCO<sub>2</sub>) synthesis is an appealing method for overcoming the aforementioned constraints. SCCO<sub>2</sub> fluid is characterized by its extremely low viscosity, gas-like diffusivity, and excellent mass transfer properties.<sup>[21]</sup> The near-zero surface tension of SCCO<sub>2</sub> allows excellent penetration between nanoparticles and the transport of reaction precursors throughout a sample.<sup>[22]</sup> The physicochemical properties of SCCO<sub>2</sub>, such as, density, viscosity, and the dielectric constant, can be tuned via temperature and pressure.<sup>[23]</sup> The control of coating layers can thus be achieved. Moreover, SCCO<sub>2</sub> is stable, nonflammable, non-toxic, and inexpensive; thus, the synthesis process is green and readily scalable. SCCO<sub>2</sub> has been used to exfoliate graphite, MoS<sub>2</sub>, and MoSe<sub>2</sub> to produce two-dimensional nanosheets for various applications.<sup>[24,25]</sup> It was also reported that SCCO<sub>2</sub> fluid could help disperse Si nanoparticles between graphene nanosheets.<sup>[26]</sup> The resulting silicon/graphene composite showed promising rate capability and cycling stability as a LIB anode. In addition, SCCO<sub>2</sub> fluid can act as a precursor carrier for the fabrication of various nanomaterials. For example, nano-size Ni,<sup>[27]</sup> Fe,<sup>[28]</sup> Pd,<sup>[22]</sup> Pt,<sup>[29]</sup> Au,<sup>[30]</sup> MnO<sub>2</sub>,<sup>[31]</sup> SnO<sub>2</sub>,<sup>[32]</sup> V<sub>2</sub>O<sub>5</sub>,<sup>[33]</sup> Fe<sub>3</sub>O<sub>4</sub>,<sup>[34]</sup> Co<sub>3</sub>O<sub>4</sub><sup>[35]</sup> have been synthesized and anchored on various nanostructured carbon materials. In addition, our team has demonstrated that SCCO<sub>2</sub> itself can serve as the precursor in the synthesis of a highly porous CoCO<sub>3</sub>/graphene nanocomposite anode for Li<sup>+</sup> and Na<sup>+</sup> storage.<sup>[36]</sup> The charge–discharge properties were superior to those of the conventionally synthesized CoCO<sub>3</sub> counterpart. To the best of our knowledge, using SCCO<sub>2</sub> to create coating layers on Si particles has not been previously attempted. We believe that this approach is worthy of investigation.

In the present work, three kinds of carbon precursor, namely, glucose, sucrose, and citric acid, are used in the SCCO<sub>2</sub>-assisted deposition process to produce carbon coating layers. SCCO<sub>2</sub> fluid can oxidize Si, producing a SiO<sub>x</sub> shell around the Si core.

A SiO<sub>x</sub>/carbon multi-layer coating on Si is thus formed in a one-pot and single-step process, which is facile and easily scaled up for mass production. A control sample synthesized using a conventional wet-chemical route without SCCO<sub>2</sub><sup>[37]</sup> is examined for comparison. The microstructure, crystallinity, chemical composition, and lithiation–delithiation behavior of various electrodes are systematically investigated. In addition, the effects of carbon precursors on the material and electrochemical characteristics are explored. The proposed SCCO<sub>2</sub> synthesis approach can fabricate high-capacity, high-power, and long-life Si@SiO<sub>x</sub>@C composite anodes for next-generation LIBs.

## 2. Results and Discussion

Figure 1a shows the X-ray diffraction (XRD) patterns of the coated Si samples and pristine bare Si powder. The peaks at 28.4°, 47.4°, 56.1°, 69.2°, and 76.3° are indexed as the (111), (220), (311), (400), and (331) plane diffraction, respectively, of cubic-structure Si (JCPDS-27-1402). The coating layers have low crystallinity and thus do not show distinct diffraction signals. Figure 1b shows the obtained Raman spectra of the coated Si samples. The peaks at 300, 520, and 960 cm<sup>-1</sup> are associated with the vibration bands of polycrystalline Si.<sup>[38]</sup> All the specimens exhibit a carbon D-band signal at ≈1345 cm<sup>-1</sup> and a carbon G-band signal at ≈1595 cm<sup>-1</sup>.<sup>[39]</sup> The former is related to imperfect carbon bonding and the latter results from the Raman-allowed in-plane vibration of sp<sup>2</sup> carbon. The carbon content of the samples was quantitatively detected by TGA; the data are shown in Figure 1c. All the specimens underwent clear weight loss at around 550–700 °C due to the burnout of the carbon layers. The data indicate that the carbon content of the T-G, SC-G, SC-S, and SC-CA samples was around 10 wt%.

Figure S1a–d, Supporting Information, show low-magnification TEM images of various samples. For T-G, aggregated Si particles can be observed. Because the particles were not de-bundled, due to relatively high surface tension and low permeability of the ethanol solvent, the carbon coating did not cover all Si particles. In contrast, with the aid of SCCO<sub>2</sub>, which has exceptional penetration ability, the Si particles were better dispersed. Figure 1d–g show high-resolution TEM images of various coated Si samples. The highly crystalline nature of the Si is confirmed by the lattice image and electron diffraction pattern shown in the figure insets. The conventional wet-chemical method produced a non-uniform carbon coating. The thickness was inhomogeneous, and we found that many places even had no carbon coverage. In contrast, the coating layer of SC-G was the most uniform and conformal, with a thickness of ≈5 nm. Sucrose has a lower solubility than glucose in ethanol.<sup>[40,41]</sup> Thus, the uniformity of the carbon film on SC-S is somewhat worse than that of SC-G. The carbon layer on SC-CA had a rough surface, which is probably related to the etching effect of citric acid toward carbon.

Figure 1h–l shows the results of the dynamic light scattering (DLS) measurements. According to the particle size distribution profiles, the D<sub>50</sub> values of the bare Si particles, T-G, SC-G, SC-S, and SC-CA are ≈125, 220, 145, 190, and 178 nm, respectively. The carbon coating film formed by SCCO<sub>2</sub> with the glucose precursor is the most compact and conformal, resulting

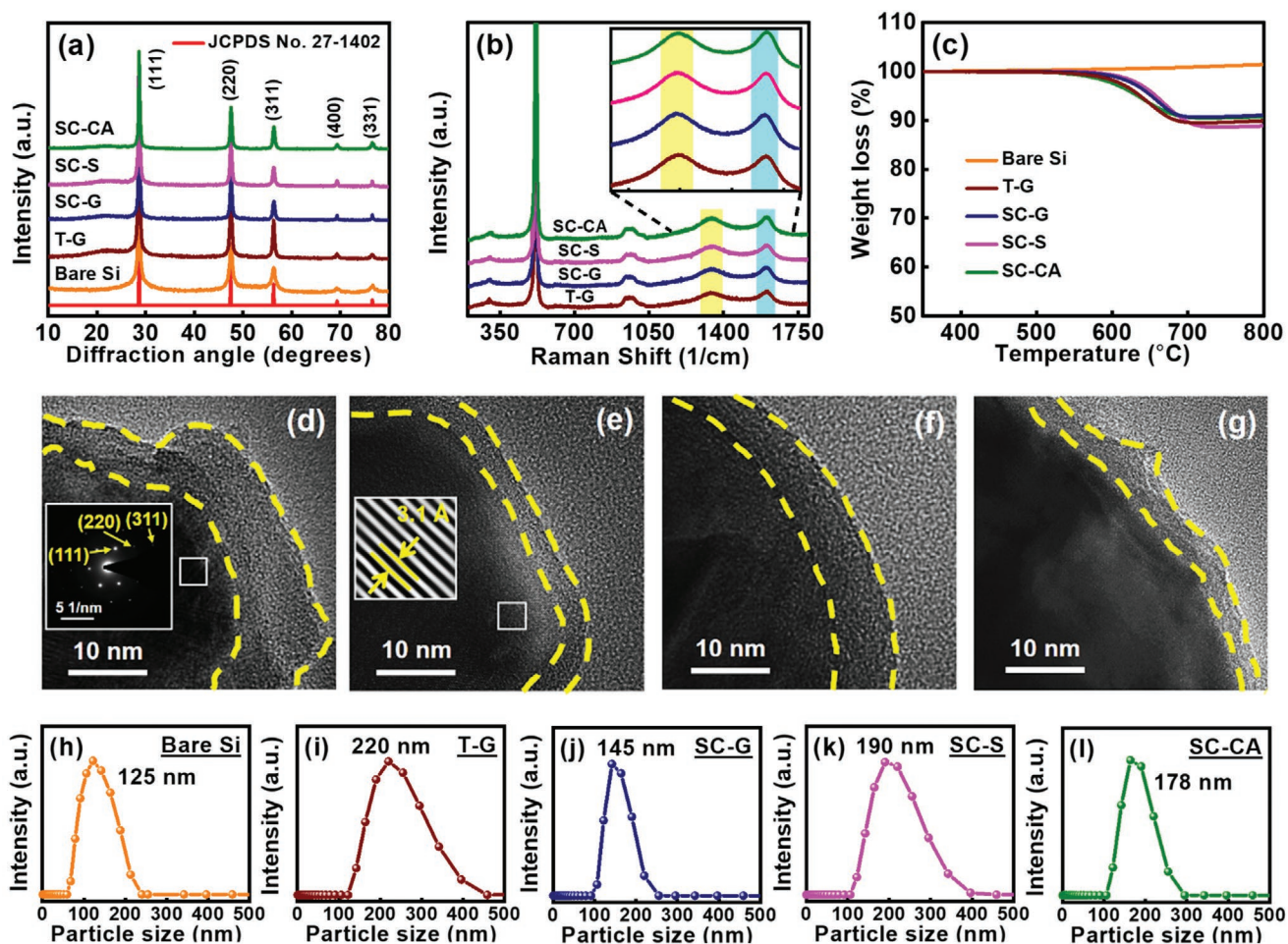


**Figure 1.** a) XRD patterns, b) Raman spectra, and c) TGA curves of bare Si and various coated Si samples. High-resolution TEM images of d) T-G, e) SC-G, f) SC-S, and g) SC-CA. Particle size distribution data of h) bare Si, i) T-G, j) SC-G, k) SC-S, and l) SC-CA measured using DLS.

in the smallest  $D_{50}$  value. In the DLS measurements, it is difficult to ensure all the particles are completely dispersed. Due to some agglomeration, the particle size and the calculated carbon layer thickness can be overestimated. The tap densities of T-G, SC-G, SC-S, and SC-CA were found to be around 0.57, 0.75, 0.67, and 0.70  $\text{g cm}^{-3}$ , respectively. The loose and uneven carbon layer on T-G creates empty space and thus decreases the packing density. The tight stacking (due to the thin and uniform coating) of the SC-G particles leads to the highest density, which is beneficial for electrode volumetric performance. It is noted that the tap density of SC-G is higher than those of silicon nanoparticles (0.16  $\text{g cm}^{-3}$ ),<sup>[42]</sup> mesoporous Si (0.25  $\text{g cm}^{-3}$ ),<sup>[43]</sup> carbon-coated Si composite (0.49  $\text{g cm}^{-3}$ ),<sup>[44]</sup> pomegranate Si particles (0.53  $\text{g cm}^{-3}$ ),<sup>[45]</sup> micro-size carbon-coated Si powder (0.68  $\text{g cm}^{-3}$ ),<sup>[46]</sup> and ball-milled Si powder (0.7  $\text{g cm}^{-3}$ ).<sup>[47]</sup>

The bulk chemical compositions of the coated samples were evaluated using scanning electron microscopy (SEM)/energy-dispersive X-ray spectroscopy (EDS) (with an analytic depth of a few microns). The data in Table S1, Supporting Information, indicate that the samples have similar Si, C, and O concentrations. Table 1 shows the surface compositions examined with X-ray photoelectron spectroscopy (XPS) at an analytic depth of a few nanometers. The results reveal that the C and O content

is higher than that measured with SEM/EDS, reflecting the enrichment of these two components near the sample surface. Figure 2a shows the XPS C 1s spectra of the samples, which are split into three peaks. In addition to the main C–C bonding peak at 284.7 eV, C–O and O–C=O signals at 286.2 and 288.7 eV, respectively, can be observed.<sup>[48,49]</sup> Fewer oxygen-containing functional groups were found on the SCCO<sub>2</sub> samples than on T-G. In addition, the carbon precursor type affected the oxygen concentrations, as shown in Table 1. SC-G had fewer C–O and O–C=O groups compared to SC-S. Sucrose molecule is a combination of glucose and fructose. The glycosidic linkage between the glucose and fructose blocks makes sucrose relatively difficult to decompose during pyrolysis.<sup>[50]</sup> In contrast, glucose molecules are readily reducible, resulting in the

**Table 1.** Elemental composition (at%) of various coated samples examined with XPS.

Element	T-G [at%]	SC-G [at%]	SC-S [at%]	SC-CA [at%]
Si	39.7	39.2	38.8	40.3
C	40.7	50.7	48.7	44.5
O	19.6	10.1	12.5	15.2



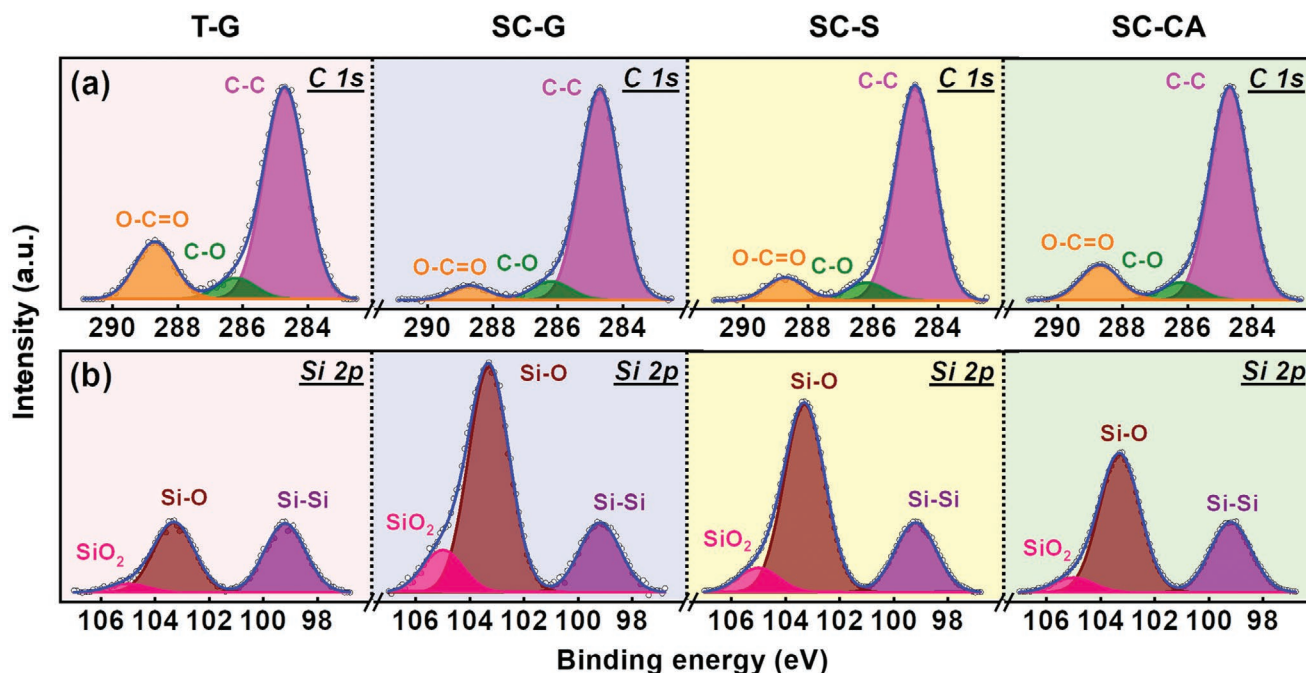
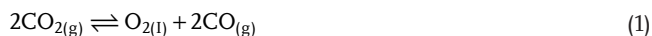


Figure 2. XPS a) C 1s and b) Si 2p spectra of various samples.

higher C–C ratio. SC-CA had the highest oxygen concentration (Table 1) among the SCCO<sub>2</sub> samples. This can be attributed to citric acid oxidizing the carbon. Moreover, the citric acid molecule consists of three carboxyl groups. Incomplete decomposition during heat treatment can result in high oxygen-containing functional group content of the carbon film.

The measured electronic conductivity values of the T-G, SC-G, SC-S, and SC-CA samples are  $2.45 \times 10^{-1}$ ,  $3.35 \times 10^{-1}$ ,  $2.97 \times 10^{-1}$ , and  $2.82 \times 10^{-1}$  S cm<sup>-1</sup>, respectively. Compared to the carbon produced via the conventional wet-chemical method, the SCCO<sub>2</sub>-derived carbon layers showed considerably higher conductivity. It is noted that a lower oxygen concentration on the sample surface (Table 1) resulted in higher electronic conductivity.

Figure 2b shows the Si 2p spectra of various samples, which can be deconvoluted into three components. The characteristic peaks at 99.3, 103.3, and 105.0 eV are associated with Si, SiO, and SiO<sub>2</sub> species, respectively. As shown, the SiO and SiO<sub>2</sub> peaks for SCCO<sub>2</sub> samples are clearly higher than those for T-G. The increased SiO<sub>x</sub> concentration probably originates from contact between the oxidizing SCCO<sub>2</sub> fluid and Si particles. The possible oxidation mechanism is proposed as follows.<sup>[51]</sup>



The O<sub>2(l)</sub> represents the interstitial oxygen molecule within the oxide. It has been found that the oxidation rate is mainly governed by the partial pressure of CO<sub>2(g)</sub>.<sup>[51]</sup> The glucose precursor has smaller molecular size and higher solubility than those of sucrose, thus decreasing the chance of blocking the interaction between SCCO<sub>2</sub> and Si. As a consequence, the SiO<sub>x</sub> concentration of SC-G is higher than that of SC-S. It was reported that

citric anions can dissolve silica.<sup>[52]</sup> Therefore, SC-CA has relatively low SiO<sub>x</sub> content. The SiO<sub>x</sub> in the T-G sample is associated with native oxide formed during exposure to the ethanol dispersion solution and ambient environment (see Section 4 for details). Although Table S1, Supporting Information, shows that all samples had similar overall oxygen concentrations, the oxygen distribution in the samples differs. For instance, T-G has its oxygen mostly bonded with carbon, whereas SC-G has fewer oxygen-containing functional groups on carbon but a higher SiO<sub>x</sub> concentration.

Figure 3a,b show high-resolution TEM analyses of the T-G and SC-G samples, respectively. For T-G, there are two separate regions in the EDS line-scan data, namely a Si core and a carbon coating layer, which has a considerable amount of oxygen. This is consistent with the XPS data. For SC-G, three distinct regions can be observed. On the Si core, there is an intermediate SiO<sub>x</sub> layer. The observed lattice fringes are in agreement with the *d* spacing of SiO (220) (JCPDS #30-1127), as shown in the inset of Figure 3b. Combining the results of high-resolution TEM and EDS elemental analysis, the intermediate layer is supposed to be a silicon oxide layer. Because the electron beam passed through the sample in the TEM analysis, the carbon signal existed across the particle. In the outer shell, there is a carbon layer with low oxygen content, which coincides with the low oxygen-containing function group concentration found in XPS. A multi-layer coating structure, that is, Si@SiO<sub>x</sub>@C, constructed via the unique SCCO<sub>2</sub> process (Figure 4) is thus confirmed. The thickness of the SiO<sub>x</sub> layer can be controlled by SCCO<sub>2</sub> pressure, reaction time, temperature, etc. The details are under investigation and will be discussed elsewhere in the future.

To investigate the electrochemical properties of various electrodes, CV measurements were performed. Figure 5a–d show the obtained CV curves of T-G, SC-G, SC-S, and SC-CA

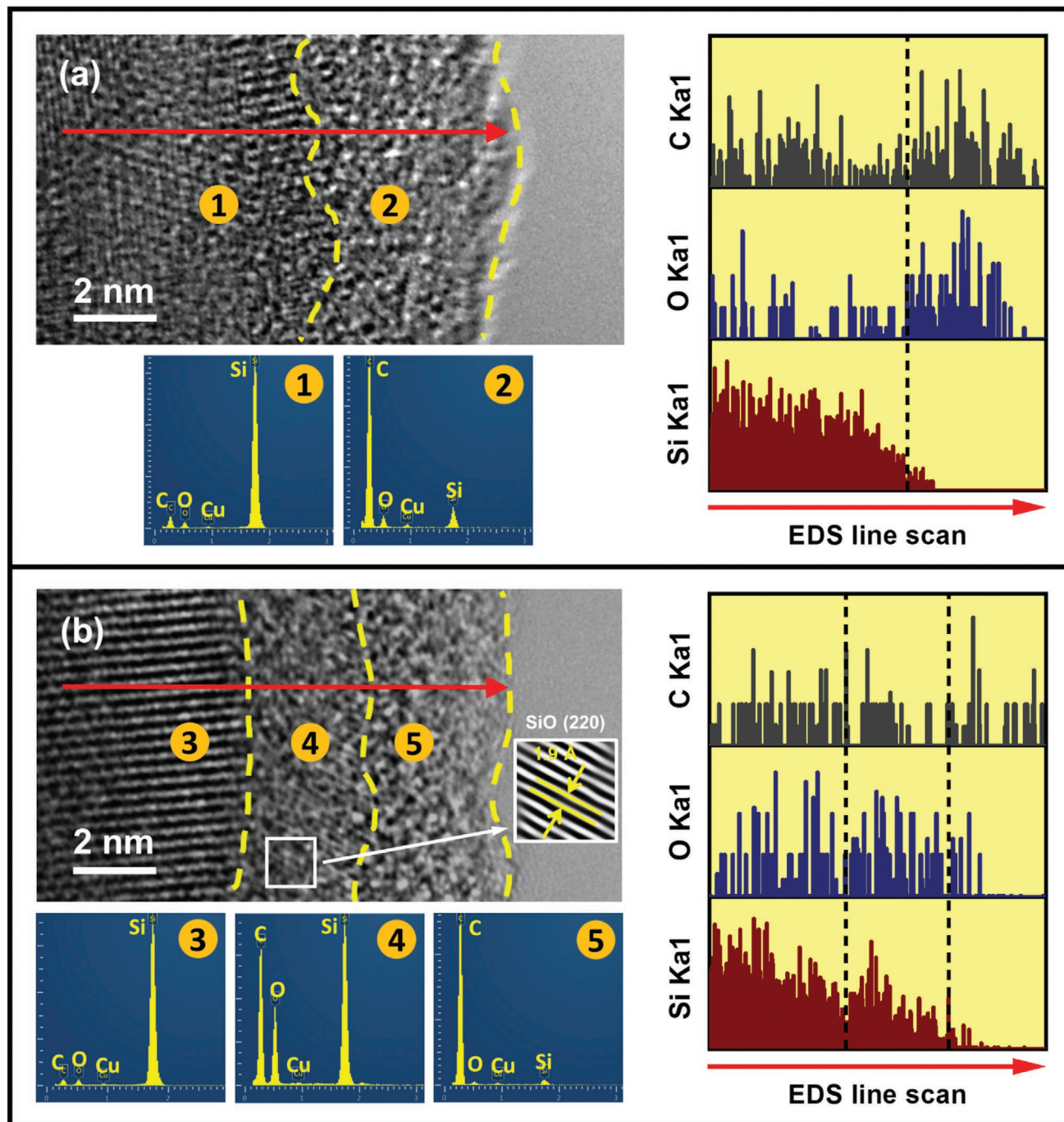


**Figure 3.** High-resolution TEM images, EDS spectra, and EDS line-scan data of a) T-G and b) SC-G samples. The EDS spectra are taken at the positions labeled in the TEM images.

electrodes. During the first cathodic scan, cathodic peaks appeared at  $\approx 1.2$  and  $\approx 0.1$  V for all electrodes. The peak at  $\approx 1.2$  V can be assigned to the reductive decomposition of the electrolyte,<sup>[53]</sup> leading to the formation of an SEI layer.<sup>[54]</sup> The peak near 0.1 V can be ascribed to the evolution of various Li-Si alloy phases.<sup>[55]</sup> During subsequent cycles, the CV shapes varied due to the electro-activation process.<sup>[56]</sup> Specifically, the cathodic alloying reactions were promoted to less negative potentials with increased current densities.

Upon the anodic scan, two distinct peaks emerged at 0.35 and 0.52 V, which correspond to the phase transition from  $\text{Li}_{15}\text{Si}_4$  to amorphous  $\text{Li}_x\text{Si}$  and that from amorphous  $\text{Li}_x\text{Si}$  to Si, respectively.<sup>[55]</sup> The elevated anodic current densities of both peaks indicate an improvement in the de-alloying kinetics upon cycling.<sup>[57]</sup> Of note, the SC-G electrode reached the saturated CV current after only three cycles, reflecting its superior electronic and ionic conductivity. However, a slow activation process was found for the T-G and SC-CA

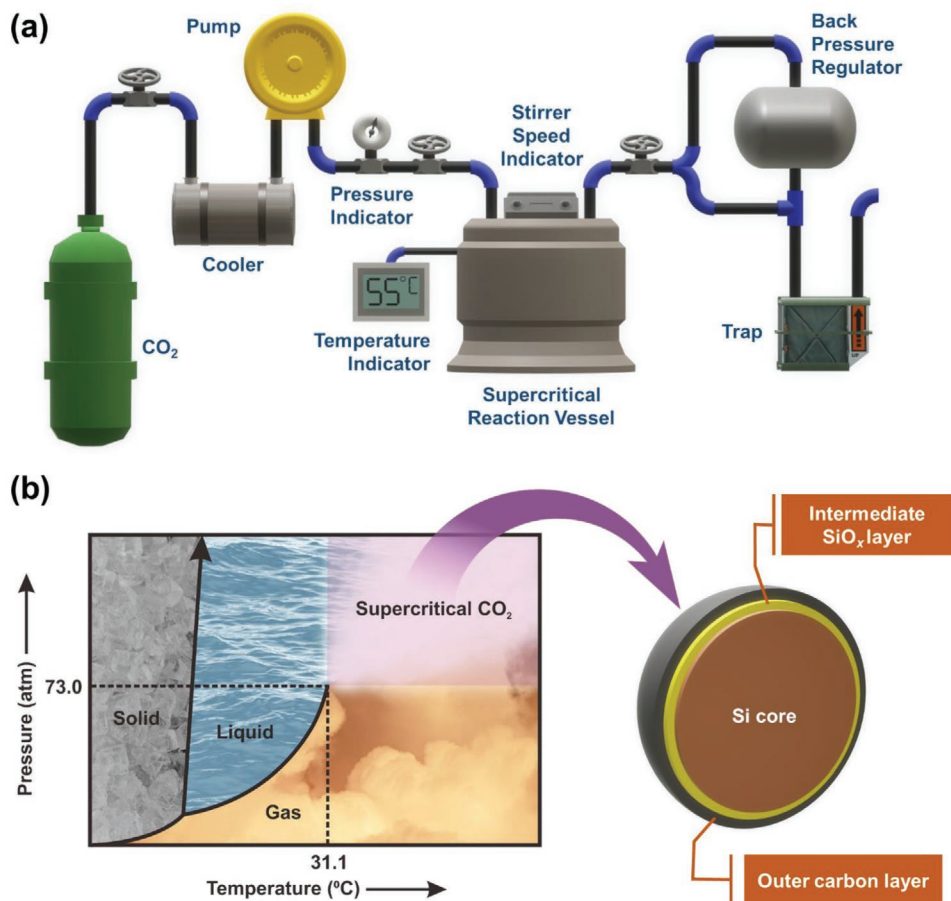


**Figure 4.** Schematic illustration of a) SCCO<sub>2</sub> apparatus. b) Phase diagram of CO<sub>2</sub> and scheme of SCCO<sub>2</sub>-fabricated Si@SiO<sub>x</sub>@C particle.

electrodes, whose CV current still increased substantially at the 5th scan cycle.

Figure S2a–d, Supporting Information, show the initial charge–discharge curves of various Si electrodes measured at a current rate of 0.2 A g<sup>-1</sup>. As shown in Table S2, Supporting Information, the first-cycle CE values of the T-G, SC-G, SC-S, and SC-CA electrodes are 75%, 84%, 82%, and 79%, respectively. SC-G had the highest CE, which can be attributed to its compact carbon coating layer with fewer oxygen-containing functional groups. An uneven and rough coating can increase surface area, increasing SEI formation.<sup>[5]</sup> The functional groups can irreversibly trap and thus consume some Li<sup>+</sup> during initial lithiation.<sup>[58]</sup> Both are unfavorable for the first-cycle CE. Moreover, SC-G has the highest electronic conductivity, which could promote the reaction reversibility and thus the CE value. It was reported that the initial CE for SiO<sub>x</sub> compounds is usually unsatisfactory;<sup>[20]</sup> however, with the aid of the SCCO<sub>2</sub>/glucose-deposited carbon layer, the first-cycle CE value of SC-G is among the best values reported in the literature, as shown in Table S3, Supporting Information. The thickness of the SiO<sub>x</sub> layer is ≈3 nm (Figure 3b). Accordingly, the Si/SiO<sub>x</sub> volume ratio is 86.8/13.2 (given the Si average particle size of 125 nm). Since the SiO<sub>x</sub> fraction is minor, the initial CE seems to be dominated by the morphology and oxygen-containing functional group concentration of the carbon coating layer. It is noted that

a high initial CE is a crucial factor for Si-based anodes that determines their practical applicability.

Figure 6a–d show the lithiation–delithiation potential profiles of various electrodes measured at various current rates after two conditioning cycles. The reversible capacities obtained at 0.2 A g<sup>-1</sup> are 1792, 2151, 1981, and 1846 mAh g<sup>-1</sup> for the T-G, SC-G, SC-S, and SC-CA electrodes, respectively. With increasing current rate, the specific capacities decreased, as shown in Figure 6e and Table S2, Supporting Information. The values of these electrodes decreased to 461, 918, 594, and 507 mAh g<sup>-1</sup>, respectively, at a specific current of 5 A g<sup>-1</sup>, corresponding to 25%, 43%, 30%, and 27% of the capacities found at 0.2 A g<sup>-1</sup>. This confirms that the coating method and carbon precursor affect the electrode rate capability. The SCCO<sub>2</sub> fluid can well de-bundle Si particles (Figure S1, Supporting Information) and then form an effective carbon conducting network within the electrodes. Moreover, the thin and conformal carbon coating on SC-G makes the powder closely connected, benefiting electron and Li<sup>+</sup> transport. As a result, superior high-rate performance of the SC-G electrode was obtained.

Figure 6f shows the electrochemical impedance spectroscopy (EIS) data of various electrodes acquired after two conditioning cycles. The Nyquist spectra consist of a semicircle at high frequency followed by a sloping line at low frequency, which can be characterized by the equivalent circuit shown in the figure



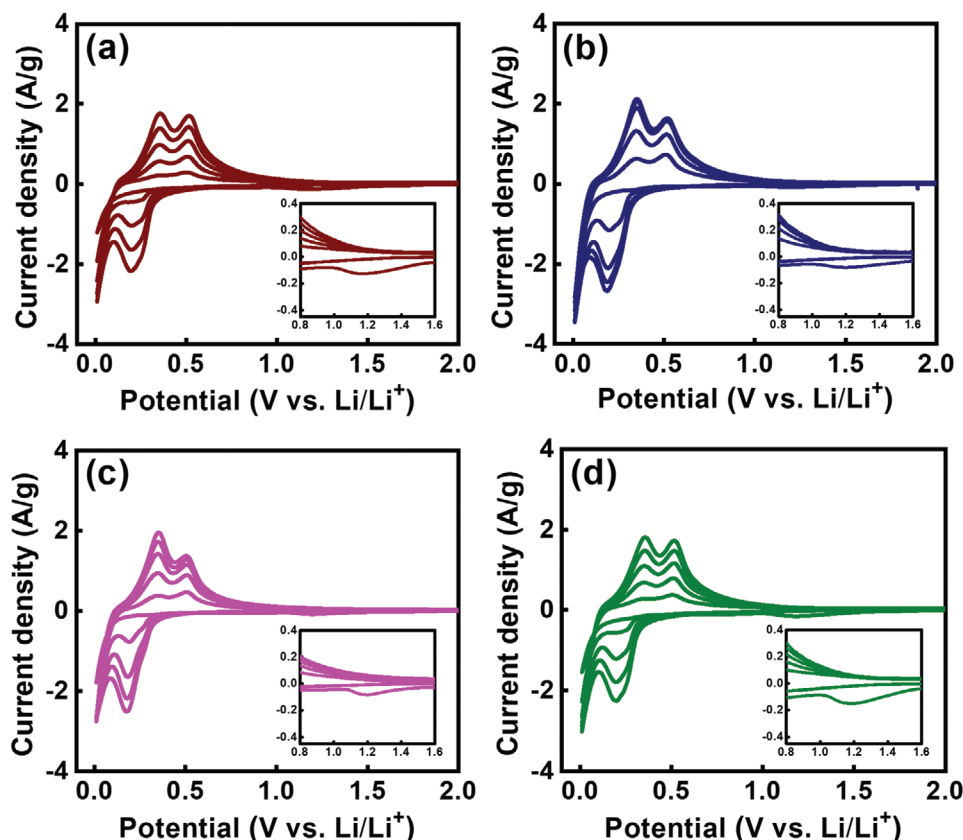


**Figure 5.** CV curves of a) T-G, b) SC-G, c) SC-S, and d) SC-CA electrodes measured at a potential sweep rate of  $0.1 \text{ mV s}^{-1}$ .

inset.  $R_e$ ,  $R_{ct}$ , CPE, and  $W$  represent the electrolyte resistance, charge transfer resistance, interfacial constant phase element, and Warburg impedance associated with  $\text{Li}^+$  diffusion within the electrode, respectively.<sup>[32]</sup> As shown in Table 2 the  $R_{ct}$  values are 43, 28, 31, and 33  $\Omega$  for the T-G, SC-G, SC-S, and SC-CA electrodes, respectively. SC-G having the lowest impedance of charge transfer can be attributed to its superior carbon coating quality and optimal conductivity. The  $\text{Li}^+$  transport properties within various electrodes were evaluated using galvanostatic intermittent titration technique (GITT). The obtained results are shown in Figure 6g,h and Figure S3, Supporting Information, and the calculated  $D_{\text{Li}^+}$  values are summarized in Table 2. The SC-G electrode has the highest  $D_{\text{Li}^+}$  value, followed by the SC-S, SC-CA, and T-G electrodes. The continuous carbon coating with fewer oxygen-containing functional groups is favorable for fast  $\text{Li}^+$  transport. The  $D_{\text{Li}^+}$  and  $R_{ct}$  data evaluated from EIS and GITT, respectively, explain the rate capability variation between the electrodes.

Figure 7a shows the cycling stability of various electrodes measured at  $1 \text{ A g}^{-1}$ . The steady CE values are 99.6%, 99.8%, 99.7%, and 99.6% for the T-G, SC-G, SC-S, and SC-CA electrodes, respectively. After 300 charge–discharge cycles, the same electrodes retained 19%, 65%, 41%, and 24% of their initial capacities, respectively. Even with such a high capacity (i.e.,  $>1600 \text{ mAh g}^{-1}$  @  $1 \text{ A g}^{-1}$ ), which means large and fast volume change, satisfactory cycling stability was achievable for the SC-G electrode. As compared in Table S3, Supporting

Information, this performance is promising. Note that we did not optimize the electrode binder and electrolyte, and did not use alloying and sophisticated architecture designs to increase cyclability in this study. Therefore, further improvement of the electrode cycle life can be expected. The impedance evolution of the electrodes upon cycling was also measured. Figure 7b shows the EIS spectra of the electrodes after 300 lithiation–delithiation cycles. As illustrated in Figure 7c and Table 2 the  $R_{ct}$  values increase to 105, 49, 60, and 74  $\Omega$  for the T-G, SC-G, SC-S, and SC-CA electrodes, respectively, after 300 cycles. The relatively large increase of  $R_{ct}$  for the T-G and SC-CA electrodes can be explained by the postmortem SEM images shown in Figure 7d–g. The morphologies of these two electrodes were significantly distorted compared to those of the pristine electrodes (see Figure S4, Supporting Information). The Si particles significantly expanded and agglomerated. Moreover, their surfaces were covered by thick production layers. Therefore, the charge transfer reactions were hindered. In contrast, as shown in Figure 7e, the structure of the SC-G electrode was highly preserved after cycling, explaining the superior capacity and  $R_{ct}$  stability.

Figure 8 illustrates the structure evolutions of the T-G and SC-G electrodes. The former sample has an incomplete and non-uniform carbon coating (see more TEM images in Figure S5, Supporting Information), which has relatively high oxygen content and thus low electronic conductivity. Moreover, the inhomogeneous carbon layer creates voids between Si

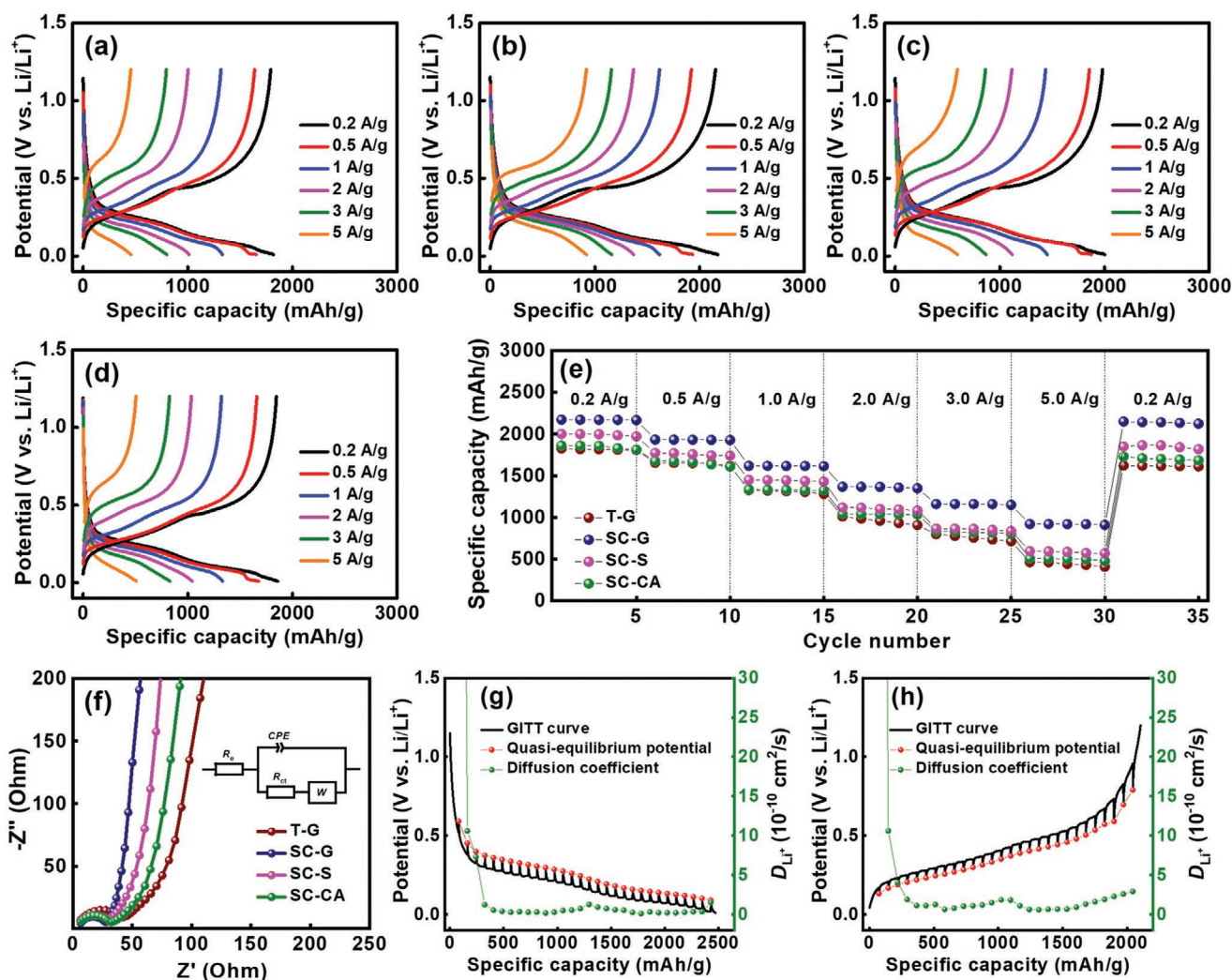


**Figure 6.** Charge–discharge curves of a) T-G, b) SC-G, c) SC-S, and d) SC-CA electrodes recorded at various current rates. e) Comparative rate performance of various electrodes. f) EIS spectra of various electrodes and equivalent circuit used for data fitting. Quasi-equilibrium potential and Li<sup>+</sup> diffusion coefficient values of SC-G electrode measured with GITT during g) lithiation and h) delithiation.

particles, decreasing the electrode material connectivity. Due to the insufficient conducting pathways, the Si volume expansion/contraction is uneven. Thus, cracks easily form and pulverization occurs. The repeated breakdown and reformation of the SEI lead to its continuous accumulation. The thickened SEI gradually isolates the loosely connected T-G particles, causing rapid capacity deterioration. After prolonged cycling, the

electrode surface is eventually covered by a massive SEI layer that hinders the charge transfer reaction and slows down the Li<sup>+</sup> transport kinetics. For SC-G, with the aid of SCCO<sub>2</sub>, the Si particles are well de-bundled and uniformly coated. As a consequence, the produced carbon layer is thin, conformal, and highly conducting. Moreover, owing to the unique interaction between SCCO<sub>2</sub> fluid and Si, a continuous SiO<sub>x</sub> transition layer

**Table 2.**  $R_{ct}$  values of various electrodes measured before and after 300 charge–discharge cycles, and  $D_{Li^+}$  values of various electrodes evaluated using GITT.

Sample	Impedance		$R_{ct}$ increase [ $\Omega$ ]	GITT results	
	after conditioning cycles	after 300 cycles		Delithiation $D_{Li^+}$ [ $\text{cm}^2 \text{S}^{-1}$ ]	Lithiation $D_{Li^+}$ [ $\text{cm}^2 \text{S}^{-1}$ ]
	$R_{ct}$ [ $\Omega$ ]	$R_{ct}$ [ $\Omega$ ]			
T-G	43	105	62	$2.26 \times 10^{-10}$	$1.15 \times 10^{-10}$
SC-G	28	49	21	$8.21 \times 10^{-10}$	$6.94 \times 10^{-10}$
SC-S	31	60	29	$4.77 \times 10^{-10}$	$2.97 \times 10^{-10}$
SC-CA	33	74	41	$3.02 \times 10^{-10}$	$1.28 \times 10^{-10}$



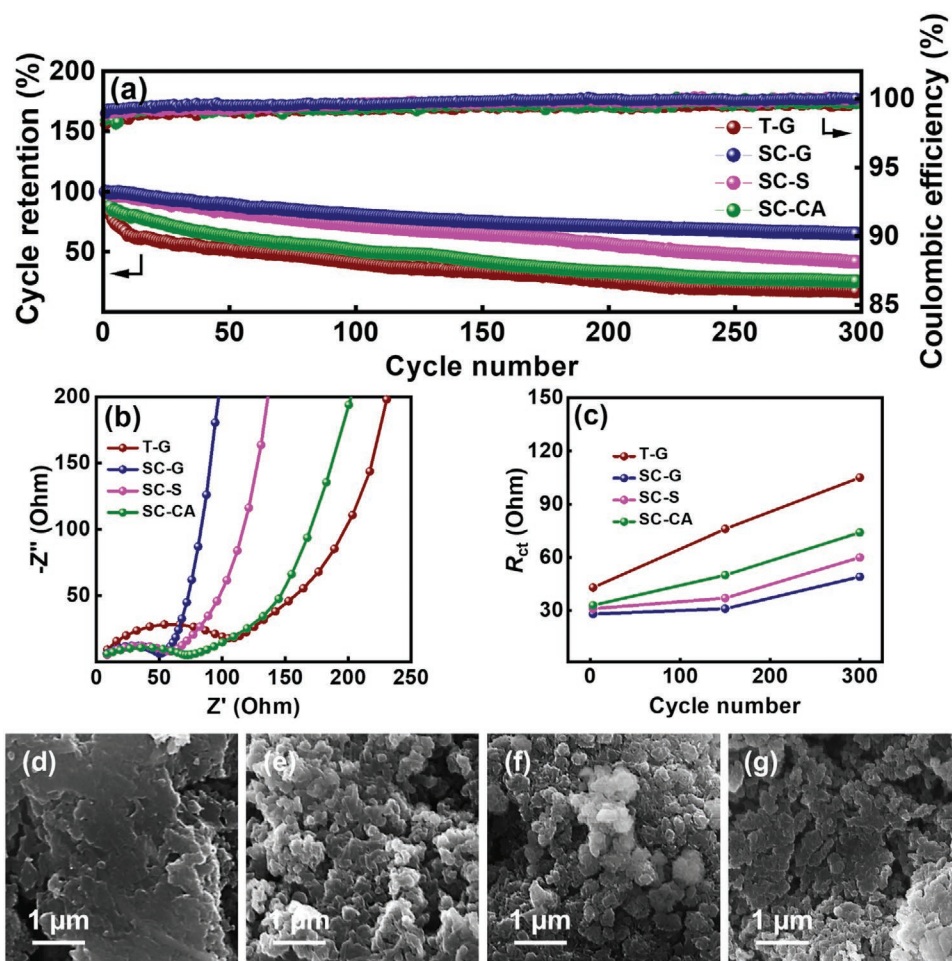


**Figure 7.** a) Cycling stability of various electrodes measured at  $1 \text{ A g}^{-1}$ . b) EIS spectra of various electrodes after 300 charge–discharge cycles. c)  $R_{ct}$  values of various electrodes with respect to charge–discharge cycle number. SEM images of d) T-G, e) SC-G, f) SC-S, and g) SC-CA electrodes after cycling.

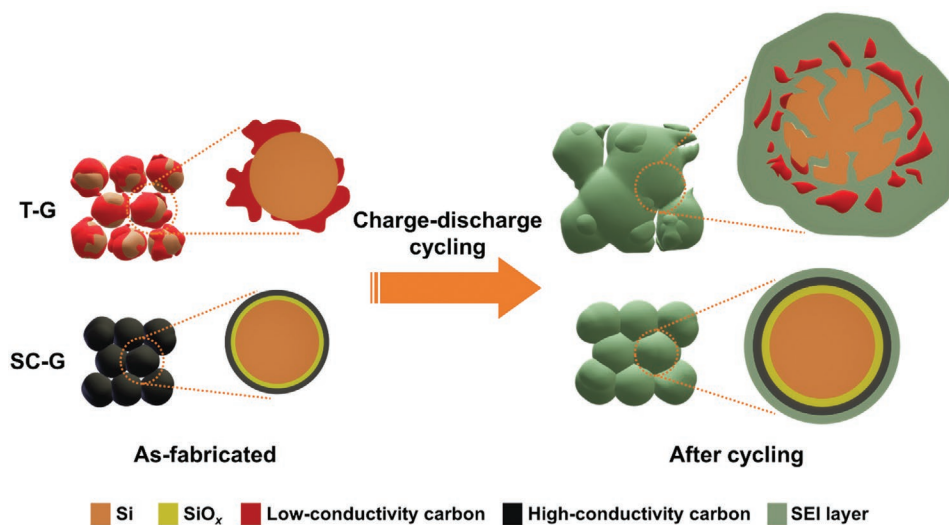


**Figure 8.** Schematic illustration of T-G and SC-G electrode morphologies before and after charge–discharge cycling.

forms between the Si core and the carbon shell. This SiO<sub>x</sub> layer buffers the Si volume change during lithiation/delithiation, and thus stabilizes the interfacial SEI.<sup>[20]</sup> Therefore, the SC-G electrode retains its structural integrity after cycling.

An SC-G||LiNi<sub>0.8</sub>Co<sub>0.1</sub>Mn<sub>0.1</sub>O<sub>2</sub> full cell was constructed with an anode-to-cathode capacity ratio of 1.1. Figure S6, Supporting Information, shows the charge and discharge profiles measured at 0.1 C. The energy density of the full cell based on the total mass of anode and cathode active materials is estimated to be ≈555 Wh kg<sup>-1</sup>, which indicates the merit of the proposed anode.

### 3. Conclusions

A SCCO<sub>2</sub> coating method for producing SiO<sub>x</sub>/carbon multilayers on Si particles was developed for the first time. Owing to the gas-like diffusivity, extremely low surface tension, and excellent permeability of SCCO<sub>2</sub> fluid, a thin and conformal coating was fabricated. The oxygen-containing functional groups of the carbon film were considerably fewer than those of the carbon film produced using a conventional wet-chemical method, leading to higher electronic conductivity for the former. An intermediate SiO<sub>x</sub> layer formed once the SCCO<sub>2</sub> fluid interacted with Si particles. The unique Si@SiO<sub>x</sub>@C material was constructed in a one-pot and single-step synthesis. This process is facile, effective, and can be easily scaled up for mass production. Of note, SCCO<sub>2</sub> is stable, nonflammable, nontoxic, and inexpensive, making it suitable for practical applications. We also confirmed that the type of carbon precursor affects the chemical composition and uniformity of the SiO<sub>x</sub>/carbon coating. With a homogeneous and highly conducting carbon layer to promote the charge transfer reaction and lithiation/delithiation reversibility and a continuous SiO<sub>x</sub> layer to buffer/mitigate the mechanical strain induced by Li<sup>+</sup> uptake/release, the SC-G electrode exhibited superior charge–discharge performance. Its first-cycle CE was 84%. The SC-G electrode, which was easily activated, showed great specific capacities of 2151 and 918 mAh g<sup>-1</sup>, respectively, at 0.2 and 5 A g<sup>-1</sup>. After 300 charge–discharge cycles, the electrode retained its integrity and ≈65% of its initial capacity. The proposed anode and material design/synthesis strategy have great potential for high-energy-density and high-power-density LIB applications.

### 4. Experimental Section

**Synthesis of SiO<sub>x</sub>/Carbon Multi-Coated Si Powder:** High-purity (>99.9%) Si powder with an average diameter of ≈1.8 μm was provided by Super Energy Material Inc., Taiwan. The particle size was reduced to ≈125 nm (D<sub>50</sub>) by planetary ball milling. A SCCO<sub>2</sub>-assisted coating method was developed (Figure 4), where glucose, sucrose, and citric acid were used as the carbon precursors (the resulting materials are denoted as SC-G, SC-S, and SC-CA, respectively). The carbon precursor and Si powder in a weight ratio of 40/60 were dispersed in anhydrous ethanol solution. Then, the mixture was transferred into a SCCO<sub>2</sub> autoclave. Ethanol, which is miscible with SCCO<sub>2</sub> fluid, was used as the co-solvent. The reactor was pressurized with CO<sub>2</sub> up to 8 MPa at 55 °C, at which the CO<sub>2</sub> reached a supercritical state. The system was stirred vigorously for 1 h before the reactor was depressurized.

The resulting powder was collected and dried in an oven at 60 °C for 12 h. Subsequently, the powder was carbonized at 850 °C under an Ar atmosphere for 5 h. For comparison, a traditional wet-chemical method using a glucose precursor was employed to fabricate a control sample (denoted as T-G). The synthesis conditions were identical to those of SC-G, but without SCCO<sub>2</sub>. The glucose and Si powder were dispersed in anhydrous ethanol solution and mixed using a magnetic stirrer at 55 °C. The resulting powder was carbonized with the same heating parameters.

**Cell Assembly:** The electrode slurry was prepared by mixing 70 wt% active material powder, 20 wt% Super P, and 10 wt% sodium polyacrylate binder in deionized water. The obtained slurry was cast onto Cu foil using a doctor blade and then vacuum dried at 100 °C for 6 h. The electrode was punched to match the required dimensions of a CR2032 coin cell. The active material mass loading was ≈1.2 mg cm<sup>-2</sup>. Li foil and a glass fiber membrane were used as the counter electrode and separator, respectively. The electrolyte consisted of 1 M LiPF<sub>6</sub> salt, ethylene carbonate/diethyl carbonate mixed solvent (1:1 by volume), and 5 wt% fluoroethylene carbonate additive. The coin cell assembly was performed in an Ar-filled glove box (Vigor Tech. Co. Ltd.), where both the moisture and oxygen content levels were maintained at below 0.1 ppm. To construct an SC-G||LiNi<sub>0.8</sub>Co<sub>0.1</sub>Mn<sub>0.1</sub>O<sub>2</sub> full cell, an anode-to-cathode capacity ratio of 1.1 was used. The SC-G anode was pre-conditioned for two cycles in a half cell prior to the full cell assembly.

**Material and Electrochemical Characterizations:** The crystallinity of the samples was characterized by XRD (Bruker D2 Phaser). The Raman spectra were collected with a LabRAM HR 800 spectrometer (with an excitation laser wavelength of 633 nm). Thermogravimetric analysis (TGA; Du Pont TGA 2950) was conducted under air with a heating rate of 5 °C min<sup>-1</sup>. The morphologies, microstructures, and chemical compositions of the samples were examined using SEM (JEOL JSM-7800F Prime), transmission electron microscopy (TEM; JEOL F200), and their auxiliary EDS. The particle size was measured using DLS (Malvern Zetasizer Nano ZS), where ethanol was used as the dispersant. XPS (Thermo Fisher Scientific ESCALAB Xi<sup>+</sup>) was employed to analyze the surface chemistry of the samples. Al Kα radiation (1486.6 eV) was adopted as the X-ray excitation source. The data fitting was conducted with XPSPEAK 4.1 software. The electronic conductivity of the samples was measured with the four-point-probe method.<sup>[59]</sup> For this measurement, the T-G, SC-G, SC-S, and SC-CA slurries were coated on plastic substrates, which provided no electronic conduction and thus avoided interference. Cyclic voltammetry (CV; BioLogic BCS-810) was performed in a range of 0.01–2.0 V (vs Li/Li<sup>+</sup>) with a potential sweep rate of 0.1 mV s<sup>-1</sup>. EIS measurements were carried out in a frequency range of 10<sup>6</sup>–10<sup>-2</sup> Hz with an AC amplitude of 10 mV. The charge–discharge properties (such as, capacity, rate capability, and cycling stability) of various cells were evaluated using an Arbin BT-2043 battery tester at 25 °C. The GITT was used to assess the apparent Li<sup>+</sup> diffusion coefficient (D<sub>Li<sup>+</sup></sub>) values of various electrodes.

### Supporting Information

Supporting Information is available from the Wiley Online Library or from the author.

### Acknowledgements

The financial support provided for this work by the Ministry of Science and Technology (MOST) of Taiwan and National Yang Ming Chiao Tung University is gratefully appreciated.

### Conflict of Interest

The authors declare no conflict of interest.

## Data Availability Statement

Research data are not shared.

## Keywords

carbon precursors, green process, high-performance anodes, multi-layer coating, supercritical fluids

Received: May 1, 2021

Revised: June 13, 2021

Published online:

- [1] M. Armand, J. M. Tarascon, *Nature* **2008**, 451, 652.
- [2] J. B. Goodenough, K. S. Park, *J. Am. Chem. Soc.* **2013**, 135, 1167.
- [3] B. Scrosati, J. Garche, *J. Power Sources* **2010**, 195, 2419.
- [4] S. Liang, Y. J. Cheng, J. Zhu, Y. Xia, P. Müller-Buschbaum, *Small Methods* **2020**, 4, 2000218.
- [5] Y. Jin, B. Zhu, Z. D. Lu, N. Liu, J. Zhu, *Adv. Energy Mater.* **2017**, 7, 1700715.
- [6] X. Su, Q. L. Wu, J. C. Li, X. C. Xiao, A. Lott, W. Q. Lu, B. W. Sheldon, J. Wu, *Adv. Energy Mater.* **2014**, 4, 1300882.
- [7] B. Koo, H. Kim, Y. Cho, K. T. Lee, N. S. Choi, J. Cho, *Angew. Chem., Int. Ed.* **2012**, 51, 8762.
- [8] J. W. Choi, D. Aurbach, *Nat. Rev. Mater.* **2016**, 1, 16013.
- [9] P. G. Bruce, B. Scrosati, J. M. Tarascon, *Angew. Chem., Int. Ed.* **2008**, 47, 2930.
- [10] M. Gu, Y. He, J. M. Zheng, C. M. Wang, *Nano Energy* **2015**, 17, 366.
- [11] F. Luo, B. N. Liu, J. Y. Zheng, G. Chu, K. F. Zhong, H. Li, X. J. Huang, L. Q. Chen, *J. Electrochem. Soc.* **2015**, 162, A2509.
- [12] T. W. Kwon, J. W. Choi, A. Coskun, *Chem. Soc. Rev.* **2018**, 47, 2145.
- [13] I. H. Son, J. H. Park, S. Kwon, S. Park, M. H. Rummeli, A. Bachmatiuk, H. J. Song, J. Ku, J. W. Choi, J. M. Choi, S. G. Doo, H. Chang, *Nat. Commun.* **2015**, 6, 7393.
- [14] H. Su, A. A. Barragan, L. Geng, D. Long, L. Ling, K. N. Bozhilov, L. Mangolini, J. Guo, *Angew. Chem., Int. Ed.* **2017**, 56, 10780.
- [15] L. Tong, P. Wang, W. Fang, X. Guo, W. Bao, Y. Yang, S. Shen, F. Qiu, *ACS Appl. Mater. Interfaces* **2020**, 12, 29242.
- [16] C. Y. Zhu, K. Han, D. S. Geng, H. Q. Ye, X. B. Meng, *Electrochim. Acta* **2017**, 251, 710.
- [17] N. Garino, E. Biserni, A. L. Bassi, P. Bruno, C. Gerbaldi, *J. Electrochem. Soc.* **2015**, 162, A1816.
- [18] I. Umezū, Y. Nakayama, A. Sugimura, *J. Appl. Phys.* **2010**, 107, 094318.
- [19] J. Li, W. Liu, Y. Qiao, G. Peng, Y. Ren, Z. Xie, M. Qu, *Front. Chem.* **2020**, 8, 666.
- [20] Z. Liu, Q. Yu, Y. Zhao, R. He, M. Xu, S. Feng, S. Li, L. Zhou, L. Mai, *Chem. Soc. Rev.* **2019**, 48, 285.
- [21] J. M. Blackburn, D. P. Long, A. Cabanas, J. J. Watkins, *Science* **2001**, 294, 141.
- [22] C. Y. Chen, J. K. Chang, W. T. Tsai, C. H. Hung, *J. Mater. Chem.* **2011**, 21, 19063.
- [23] J. Patra, H. C. Chen, C. H. Yang, C. T. Hsieh, C. Y. Su, J. K. Chang, *Nano Energy* **2016**, 28, 124.
- [24] X. Wang, K. Wen, T. Chen, S. Chen, S. Zhang, *Appl. Surf. Sci.* **2020**, 522, 146507.
- [25] Q. D. Truong, M. K. Devaraju, Y. Nakayasu, N. Tamura, Y. Sasaki, T. Tomai, I. Honma, *ACS Omega* **2017**, 2, 2360.
- [26] S. H. Lee, S. Park, M. Kim, D. Yoon, C. Chanthad, M. Cho, J. Kim, J. H. Park, Y. Lee, *Sci. Rep.* **2016**, 6, 32011.
- [27] C. Y. Chen, J. K. Chang, K. Y. Lin, S. T. Chung, W. T. Tsai, *Mater. Sci. Forum* **2010**, 1148, 638.
- [28] D. H. Jiang, C. H. Yang, C. M. Tseng, S. L. Lee, J. K. Chang, *Nanoscale* **2014**, 6, 12565.
- [29] S. Yoda, A. Hasegawa, H. Suda, Y. Uchimaru, K. Haraya, T. Tsuji, K. Otake, *Chem. Mater.* **2004**, 16, 2363.
- [30] J. W. Wu, C. H. Wang, Y. C. Wang, J. K. Chang, *Biosens. Bioelectron.* **2013**, 46, 30.
- [31] M. T. Lee, C. Y. Fan, Y. C. Wang, H. Y. Li, J. K. Chang, C. M. Tseng, *J. Mater. Chem. A* **2013**, 1, 3395.
- [32] J. D. Xie, H. Y. Li, B. Umesh, T. C. Lee, J. K. Chang, Y. A. Gandomi, *Electrochim. Acta* **2018**, 292, 951.
- [33] Q. H. Do, C. Zeng, C. Zhang, B. Wang, J. Zheng, *Nanotechnology* **2011**, 22, 365402.
- [34] X. Hu, M. Ma, M. Zeng, Y. Sun, L. Chen, Y. Xue, T. Zhang, X. Ai, R. G. Mendes, M. H. Rummeli, L. Fu, *ACS Appl. Mater. Interfaces* **2014**, 6, 22527.
- [35] V. H. Nguyen, C. Kang, C. Roh, J. J. Shim, *Ind. Eng. Chem. Res.* **2016**, 55, 7338.
- [36] H. Y. Li, C. M. Tseng, C. H. Yang, T. C. Lee, C. Y. Su, C. T. Hsieh, J. K. Chang, *ChemSusChem* **2017**, 10, 2464.
- [37] B. Umesh, P. C. Rath, R. F. H. Hernandha, J. Y. Lin, S. B. Majumder, Q. F. Dong, J. K. Chang, *ACS Sustainable Chem. Eng.* **2020**, 8, 16252.
- [38] S. Schipporeit, D. Mergel, *J. Raman Spectrosc.* **2018**, 49, 1217.
- [39] Y. S. Hu, R. Demir-Cakan, M. M. Titirici, J. O. Muller, R. Schlogl, M. Antonietti, J. Maier, *Angew. Chem., Int. Ed.* **2008**, 47, 1645.
- [40] L. A. Alves, J. B. A. e Silva, M. Giuliatti, *J. Chem. Eng. Data* **2007**, 52, 2166.
- [41] M. Mathlouthi, P. Reiser, *Sucrose-Properties and Application*, Springer, Boston, MA **1995**.
- [42] S. O. Kim, A. Manthiram, *J. Mater. Chem. A* **2015**, 3, 2399.
- [43] B. R. Wang, W. W. Li, T. Wu, J. Guo, Z. Y. Wen, *Energy Storage Mater.* **2018**, 15, 139.
- [44] A. Magasinski, P. Dixon, B. Hertzberg, A. Kvit, J. Ayala, G. Yushin, *Nat. Mater.* **2010**, 9, 353.
- [45] N. Liu, Z. Lu, J. Zhao, M. T. McDowell, H. W. Lee, W. Zhao, Y. Cui, *Nat. Nanotechnol.* **2014**, 9, 187.
- [46] J. X. Song, S. R. Chen, M. J. Zhou, T. Xu, D. P. Lv, M. L. Gordin, T. J. Long, M. Melnyk, D. H. Wang, *J. Mater. Chem. A* **2014**, 2, 1257.
- [47] M. Gauthier, D. Mazouzi, D. Reyter, B. Lestriez, P. Moreau, D. Guyomard, L. Roue, *Energy Environ. Sci.* **2013**, 6, 2145.
- [48] B. Wang, T. F. Liu, A. M. Liu, G. J. Liu, L. Wang, T. T. Gao, D. L. Wang, X. S. Zhao, *Adv. Energy Mater.* **2016**, 6, 1600426.
- [49] W. W. Jiang, M. Q. Wu, F. Liu, J. Yang, T. T. Feng, *RSC Adv.* **2017**, 7, 44296.
- [50] I. Šimković, I. Šurina, M. Vričan, *J. Anal. Appl. Pyrolysis* **2003**, 70, 493.
- [51] T. Sakon, J. B. Wagner Jr., in *Proc. The Symp. on The Physics and Chemistry of SiO<sub>2</sub> and the Si-SiO<sub>2</sub> Interface* (Eds: C. R. Helms, B. E. Deal), Springer, Boston, MA, **1988**.
- [52] F. R. Bacon, F. C. Raggon, *J. Am. Ceram. Soc.* **1959**, 42, 199.
- [53] I. A. Profatilova, C. Stock, A. Schmitz, S. Passerini, M. Winter, *J. Power Sources* **2013**, 222, 140.
- [54] L. Ma, J. Q. Meng, Y. J. Cheng, Q. Ji, X. Zuo, X. Wang, J. Zhu, Y. Xia, *Chem. - Asian J.* **2020**, 15, 2674.
- [55] Y. H. Xu, Y. J. Zhu, F. D. Han, C. Luo, C. S. Wang, *Adv. Energy Mater.* **2015**, 5, 1400753.
- [56] L. Wang, T. F. Liu, X. Peng, W. W. Zeng, Z. Z. Jin, W. F. Tian, B. Gao, Y. H. Zhou, P. K. Chu, K. F. Huo, *Adv. Funct. Mater.* **2018**, 28, 1704858.
- [57] Z. Favors, W. Wang, H. H. Bay, A. George, M. Ozkan, C. S. Ozkan, *Sci. Rep.* **2014**, 4, 4605.
- [58] Y. Wang, W. Liu, R. T. Guo, Q. T. Qu, H. H. Zheng, J. Y. Zhang, Y. H. Huang, *J. Mater. Chem. A* **2019**, 7, 22621.
- [59] Y. Lu, L. M. Santino, S. Acharya, H. Anandarajah, J. M. D'Arcy, *J. Chem. Educ.* **2017**, 94, 950.